

# THE COOLING GRADIENT AND MICROSTRUCTURE CONTROL IN LASER BEAM WELDED TiAl ALLOY ASSISTED BY TEMPERATURE FIELD SIMULATION

Jie Liu\*, Peter Staron, Dirk Schnubel, Norbert Schell, Norbert Huber, Nikolai Kashaev  
Institute of Materials Research, Helmholtz-Zentrum Geesthacht

*Keywords:* TiAl alloys, Laser beam welding, FEM simulation, Residual stress

## Abstract

*Assisted by temperature field finite element simulation, TiAl-based alloys were welded and heat treated with laser systems combined with precise control of the temperature gradient in the welding zone and the heat-affected zone. The welded samples were investigated by scanning electron microscope and high-energy X-ray diffraction. It is found out that by careful control of the cooling rate, the residual stresses are largely removed in the weld seam and the microstructure is improved. Tensile tests are carried out for the comparison of the non-heated and the heat treated joints. It is proved that the mechanical properties of the joints are balanced by the careful temperature control.*

## 1 Introduction

The  $\gamma$ -TiAl materials are attractive alternative candidates for aerospace and automotive applications because of their low density ( $\sim 4 \text{ g/cm}^3$ ), high specific yield strength at high temperature, and high creep and oxidation resistance [1-4]. They are of great potential to replace nickel-based alloys intended for service at temperatures up to  $800^\circ\text{C}$  [5]. However, the low ductility and fracture toughness of  $\gamma$ -TiAl-based alloys at ambient temperature and their limited weldability restrict their industrial and commercial application. Great efforts have been made to produce sound joints of the material. However, there are still some challenges.

Longitudinal and transverse cracks were often observed in the weld seam, due to the intrinsic brittleness of the material [6, 7]. It was reported that with proper selection of the cooling rate, butt joining can be achieved for

small work pieces [7]. Also, when the  $\gamma$ -TiAl based samples are pre-heated in furnace at  $750^\circ\text{C}$ , joints can be made without cracking [8].

Due to the high cooling rate, a large amount of residual stress is produced in the welding zone (WZ), which is detrimental to the mechanical properties. The residual stresses were found to be over 1000 MPa in an as-welded specimen ( $13 \times 50 \times 2 \text{ mm}^3$ , Ti-45Al-5Nb-0.2C-0.2B, at. %, same throughout the whole manuscript) and it was reduced to 460 MPa after in situ post-weld heat treatment by a defocused laser. The residual stress was totally relieved only after the specimen was heat treated in furnace for 2 hours at  $1260^\circ\text{C}$  followed by furnace cooling [9].

The cooling rate plays an important role in microstructure transformation. The weld zone is composed of a large amount of brittle  $\alpha_2$  phase as reported by Arenas et al. on  $\gamma$ -TiAl based material (Ti-46.8Al-1.8Cr-1.8Nb-0.02Fe-0.004Si) [10]. The dendritic  $\alpha_2$  grains transform gradually into ductile equiaxed  $\gamma$  after post-weld heat treatment. Moreover, it is found that coarse lamellar dendrites could be refined to equiaxed grains when the material cools down slowly. The refined microstructure shows a good balance between tensile strength and ductility [8]. Thus, it is important to control the temperature field and the cooling rate to produce a sound weld with good mechanical properties.

The goal of the present work is to improve the welding zone microstructure and reduce the residual stress of laser beam-welded specimens via laser heat treatments. The temperature field and cooling gradient during welding and heating are controlled by temperature field measurement and simulation. Welding and heating are carried

out with optimized laser parameters. Also, the microstructure transformation mechanism according to the temperature loading cycle is discussed.

## 2 Experiments

### 2.1 Material

A  $\gamma$ -TiAl based alloy with a chemical composition of Ti-43.5Al-4Nb-1Mo-0.1B, termed as TNM, was investigated. It solidifies via the  $\beta$  phase as shown in the phase diagram displayed in Fig. 1a. During solidification the alloy undergoes a transformation pathway as  $L \rightarrow L + \beta \rightarrow \beta \rightarrow \beta + \alpha \rightarrow \alpha + \beta + \gamma \rightarrow \alpha + \beta + B2 + \gamma \rightarrow \alpha + B2 + \gamma \rightarrow \alpha + \alpha_2 + B2 + \gamma \rightarrow \alpha_2 + B2 + \gamma$ . The phase fraction diagram is depicted in Fig. 1b for the chemical composition of Ti-43.67Al-4.08Nb-1.02Mo-0.1B, which is similar to the alloy used here. It shows there is no occurrence of a single  $\alpha$  phase field region. The  $\alpha$  phase is supersaturated in the temperature

region of 1255 - 1405 °C, where  $\gamma$  is completely dissolved and  $\beta \rightarrow \alpha$  transformation takes place. When the material cools rapidly down from ( $\alpha + \beta$ ) field, a large amount of  $\alpha_2$  and B2 phases remains at room temperature (RT).

### 2.2 Welding and heating

The TNM sheets were cut by electro-discharge machining (EDM) into plates of  $25 \times 25 \times 1.5 \text{ mm}^3$  and subsequently cleaned to remove oxides and remnants. The specimen was mounted in a furnace filled with Ar gas. The specimen was preheated until 900 °C. A laser was aligned perpendicular to the specimen surface. Bead-on-plate welds were carried out along the centre line of the specimen, with a laser power of 600 W at a feed rate of 5 mm/s (specimen #1). The specimen #2 was welded in the same way as #1. A post-weld heat treatment was carried out by a defocused laser after the

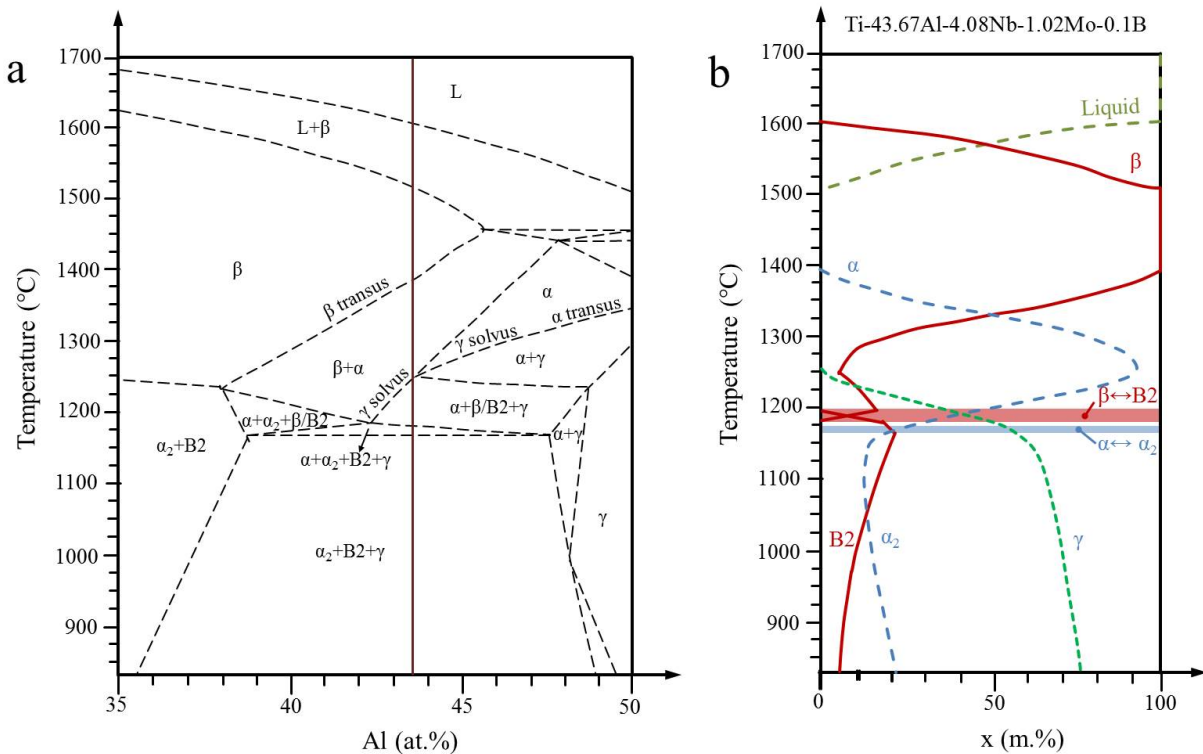


Fig. 1: (a) Experimental phase diagram of the alloy Ti-xAl-4Nb-1Mo-0.1B. The Al content of the investigated alloy is indicated as a vertical line. (b) Course of phase fractions with temperature for the investigated alloy composition Ti-43.67Al-4.08Nb-1.02Mo-0.1B [11].

## THE COOLING GRADIENT AND MICROSTRUCTURE CONTROL IN LASER BEAM WELDED TIAL ALLOY ASSISTED BY TEMPERATURE FIELD SIMULATION

specimen cooled down to 900 °C. The diameter of the defocused laser was 5 mm, which was larger than the width of the WZ and the heat-affected zone (HAZ). A laser power of 500 W with a feed rate of 5 mm/s was applied during the heating. After welding/heating both specimen #1 and #2 were held at 900 °C for 2 minutes and cooled down to RT at a rate of 12.8 °C/s.

### 2.3 Temperature measurements

As indicated in Fig. 2a, the specimen was fixed by a clamping jig and heated by ceramic heating elements. The transient temperature distribution during laser welding and heating was characterised using 8 type K thermocouples. The thermocouples were placed in blind holes produced by EDM to a depth of 1 mm from the far side of the laser. Fig. 2b shows the exact positions of the holes. The laser started at the left edge of the specimen, where P1 was located. It moves along the centre line, which is coloured in blue and finally, ends at the right edge. It is important to mention that the width of the WZ is around 3 mm. The points P1, P2, P3, P5, P7 and P8 are located at the interface of the WZ and HAZ. Two points P4 and P6 are placed 2 mm away in the HAZ to measure the temperature transverse to the weld. For data acquisition, a computer-based measurement

system with a sampling rate of 400 Hz was used.

### 2.4 Microstructure observation and residual stress measurement

The microstructure of the laser beam-welded joints was examined by scanning electron microscopy in backscattered electron mode. The mean grain size was determined by SEM image observation by a linear intercept method. The mean grain size was averaged after at least ten measurements. The residual stresses in samples were determined using X-ray diffraction at the HZG beamline HEMS (High Energy Materials Science) at Deutsches Elektronen-Synchrotron (DESY), Hamburg. The incident beam was calibrated to photon energy of 87.3 keV impinged into the 1.5 mm thick weld plate in transmission mode. The detector was oriented strictly perpendicular to the incident beam to capture diffracted 2D Debye-Scherrer cones. The cross section of the monochromatic beam was  $0.25 \times 0.25 \text{ mm}^2$  to reach a good lateral resolution at a scanning step size of 0.25 mm. The scan was performed across the weld seam with the weld seam at the middle position. Two comb-shaped reference samples were machined out of the cross section from the fusion zone by EDM at the end of each specimen in order to

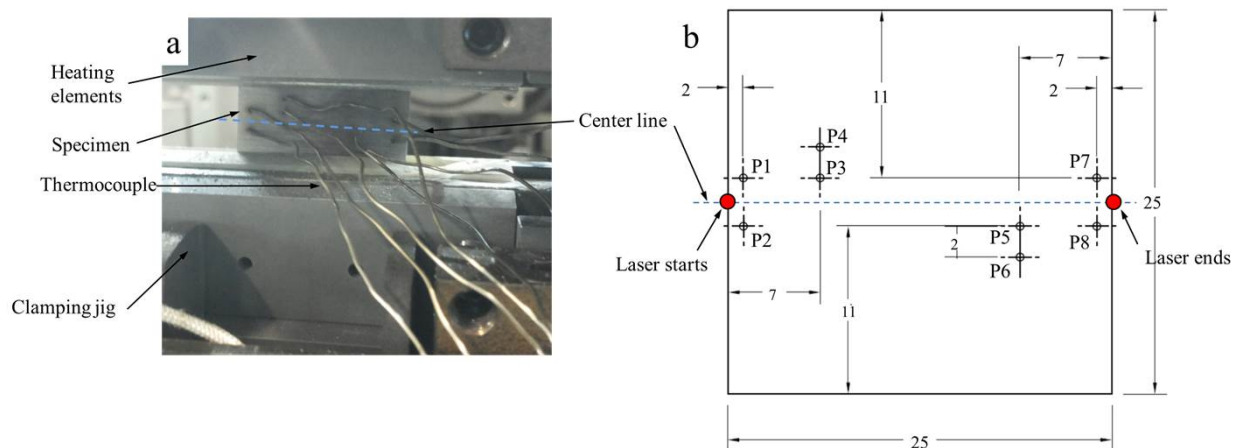


Fig. 2: (a) The experimental set-up of laser beam welding and heating. The thermocouples are placed in the holes for temperature measurement. (b) Sketch of the exact positions of the holes P1-P8. The unit is mm in the figure. The laser started at the left edge of the specimen, moves along the centre line, and finally ends at the right edge.

obtain the stress-free interplanar lattice distance  $d_0$ . It is assumed that macro-stresses were relaxed in the comb “fingers” [12].

### 2.5 Micro tensile test

The as-welded and heat-treated specimens were cut by EDM into flat micro tensile specimens for the tensile tests. The gauge dimensions of the test specimens were 27 mm × 5 mm × 1 mm. The 27mm is the gauge length, which is used in the tensile direction. The detail of the specimen geometry can be found in [8]. Specimens were ground with a 2500# SiC paper in order to minimize micro cracks on the surface. The tensile tests were carried out at both RT and 750°C in the lab air with an initial strain rate of  $1.67 \times 10^{-5}/s$ . At least three tests were performed on each condition and the average values were reported.

## 3 Results and discussions

### 3.1 Temperature field measurement and simulation

The thermal simulation was carried out by the Fine Element mode. A pure heat conduction model including heat sinks and sources was

used. The governing differential equation is given as follow:

$$\rho(T)c(T)\frac{\partial T}{\partial t} - \mathbf{div}(\lambda(T)\mathbf{grad} T) - Q = 0 \quad (1)$$

where  $T$  is the temperature,  $c$  is the specific heat,  $\rho$  is the density,  $\lambda$  is the thermal conductivity and  $Q$  is the heat flux density. The parameters  $c$ ,  $\rho$  and  $\lambda$  are temperature dependent. The heat source is described in a subroutine. Details of heat source simulation are described in [13].

The Fig. 3 presents a comparison of the thermocouple measurements and the simulation results for the nodes at the corresponding positions. The solid lines represent the experimental measurements and the hollow points show the simulation results. The temperature measurement of P7 was only carried out during heating until 1320 °C, which is the upper limit of the type K thermocouple. The comparison with the thermocouple measurements shows that the global heat input and the thermal conduction match very well with the thermal simulation. The points P1 and P7 are located at the edges of the specimen. The temperature of P1 is lower than that of P3 as the specimen starts to heat up. P7 experiences the highest temperature because it suffers heat concentration at the welding end. As indicated

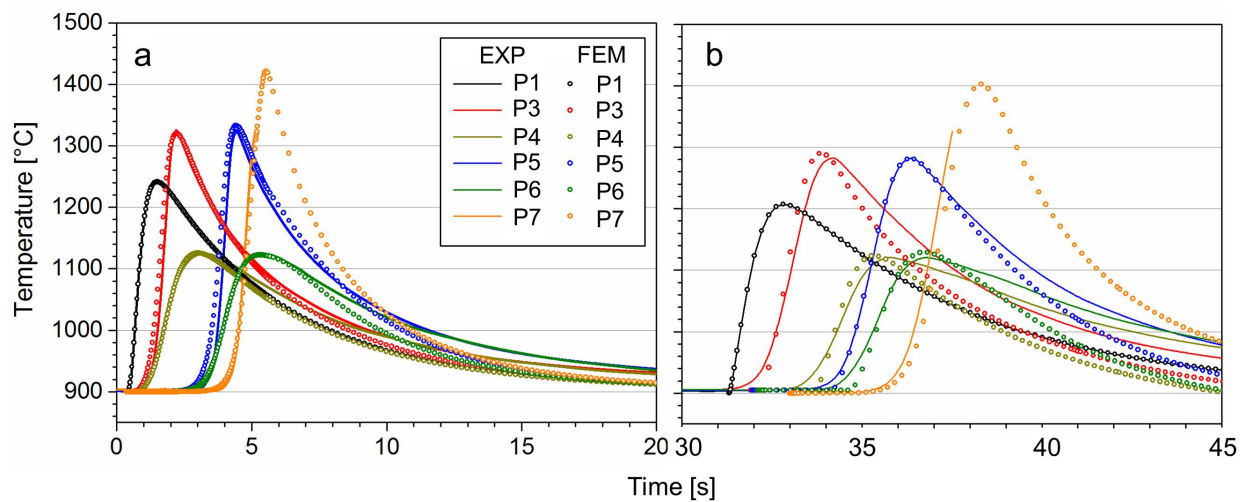


Fig. 3: Comparison of the thermocouple measurements (EXP) and the results of the thermal FE analysis (FEM) measured and simulated transient temperatures (a) during welding and (b) heating. The P1, P2 and P7, P8 are overlapping and only P1 and P7 are presented here.

by Fig. 3a, point P3, which is at the interface of the WZ and HAZ, is heated from 900 °C with a heating rate of 578 °C/s to the maximum temperature of 1325 °C and then cools down at a cooling gradient of 96 °C/s. The temperature gradient in the HAZ is much smaller in the WZ. As for P4, it reaches a peak temperature of 1124 °C at a rate of 90.9 °C/s and cools down at 14.7 °C/s. During laser heating (Fig. 3b), the WZ is heated to 1282 °C at 184.4 °C/s and cools down at 59.2 °C/s which are smaller compared to laser welding.

### 3.2 Microstructures

Fig. 4 shows the microstructure of the base material (BM), WZ and HAZ of specimen #1. The BM microstructure is shown in Fig. 4a and it is termed as “nearly lamellar  $\gamma$ ” (NL  $\gamma$ ). The  $\alpha$  grains are precipitated from the  $\beta$  phase with different orientations with respect to the parent phase. This leads to a segregation of Ti, Nb and Mo in the remaining  $\beta$  phase. Due to this enrichment of relatively heavy elements, the  $\beta$  phase appears brightly in the back-scattered SEM micrographs. It indicates that the material pass through the ( $\alpha + \beta$ ) phase field during cooling, which is considered to be beneficial for grain refinement since  $\alpha$  grain growth is restricted [14]. Subsequently, during the transformation  $\alpha \rightarrow \alpha_2 + \gamma$ , the  $\gamma$  lamellae are formed within the  $\alpha$  grains. The dimension of the equiaxial  $\alpha_2/\gamma$  colonies are about 45.8  $\mu\text{m}$  in diameter. At RT  $\alpha$  and  $\beta$  are present as ordered phases  $\alpha_2\text{-Ti}_3\text{Al}$  and  $\gamma\text{-TiAl}$  with D0<sub>19</sub>- and B2-structure, respectively. The microstructural features are better resolved in Fig. 4b. It shows the  $\alpha_2/\gamma$  colonies are surrounded by ordered B2-phase and globular  $\gamma$  grains. The globular  $\gamma$  precipitates within the B2 phase either by discontinuous coarsening or direct nucleation [14]. Also, some  $\alpha_2/\gamma$  lamellae present curve morphology within a single colony, showing a heavy deformation due to rolling.

The microstructure of the WZ is depicted in Fig. 4c. It shows acicular lamellar colonies with apparently nearly random orientations embedded in the B2 matrix. The average dimension of the acicular colony is 20.8  $\mu\text{m} \times$  2.8  $\mu\text{m}$ , which is largely refined compared to

that of the BM. The detail of the microstructure (Fig. 4d) reveals the lamellae are composed of fine-spaced  $\alpha_2/\gamma$ . The adjacent colonies do not exhibit parallel lamellae, indicating they are not stemmed from the same parent  $\alpha$ . The  $\gamma$  grains transform to small lens-shape ( $\gamma_{\text{lens}}$ ) within the B2 matrix. This type of microstructure is termed as “nearly lamellar  $\beta$ ” (NL  $\beta$ ) microstructure, which means that no globular  $\gamma$  grains is present. The boride segregation causes strong undercooling during solidification. They serve as heterogeneous nucleation sites for the  $\alpha$  phase and lead to lamellar refinement during the  $\beta/\alpha$  transformation [15]. However, the grain refinement through borides is dependent on the cooling rate. It is indicated by Oehring et al. [16] and Liu et al. [17] that heterogeneous nucleation of  $\alpha$  phase at borides is promoted by slow cooling rates (1 °C/s) and suppressed by high cooling rates (air cooling). Although there is no temperature curve of the WZ depicted in this study, the temperature gradient at the interface of WZ/HAZ is measured in Fig. 3. It shows the WZ/HAZ interface cools down from 1325 °C to 1255 °C at a cooling rate of 96 °C/s. Although the  $\alpha$  grains stem from the same  $\beta$ , they can present different orientations, due to the Burgers orientation relationship,  $\{110\}_{\beta} // (0001)_{\alpha}$  and  $\langle 111 \rangle_{\beta} // \langle 11-20 \rangle_{\alpha}$ . The  $\alpha$  grains precipitate from  $\beta$  with 12 variants, which leads to lamellae of different orientations. Also the  $\gamma_{\text{lens}}$  are in the same direction as the lamellae. It is speculated the lens-shaped  $\gamma$  is formed by discontinuous coarsening.

The microstructure of the HAZ is presented in Fig. 4e-f. The  $\alpha_2/\gamma$  lamellar grains show two kinds of morphologies, either equiaxial or acicular. The equiaxial colonies of 22.3  $\mu\text{m}$  in diameter are surrounded by the acicular lamellae with a dimension of 8.5  $\mu\text{m} \times$  1.2  $\mu\text{m}$ . The  $\gamma$  grains are in both globular and lens-shape. The acicular lamellae and  $\gamma$  grains are homogeneously distributed in the B2 matrix. From microstructural point of view, it is interesting to point out that equiaxial colonies are in the same morphology as in the BM but with a smaller size. Also the profile of the acicular lamellae is the same as that in the WZ. It can be indicated that the HAZ is heated to ( $\alpha + \beta$ ) or single  $\beta$  filed for a short time. The

globular  $\gamma$  grains in the inter-colony area first dissolve due to their high Al content. They invade into lamellar colonies and reduce the lamellar dimension. When the HAZ cools down, the supersaturated  $\alpha$  grains decompose to  $\alpha_2 + \gamma$  lamellae. The  $\gamma$  is formed by precipitation in B2 or coarsening from the  $\gamma$  lath in the lamellae.

The temperature diagram of the HAZ (Fig. 3b) also verifies that the HAZ experienced a peak temperature of 1325 °C, which is in the ( $\alpha + \beta$ ) phase field. The phase transformation corresponds well with the temperature measurement.

The microstructure after laser heating is shown in Fig. 5. The WZ presents randomly distributed lamellar microstructure of dimension of  $28.2 \mu\text{m} \times 3.2 \mu\text{m}$ . It is shown that the acicular lamellar colonies are coarsened after the laser heating. The amount of B2 phase in the inter lamellae region is smaller than the as-welded WZ. As the B2 phase is reported to be brittle at RT, the reduction of its amount is helpful to increase the elongation to fracture. In the HAZ, the globular  $\gamma$  grains are located in the B2 matrix. It is observed that the  $\gamma$  grains grow to 3  $\mu\text{m}$  in length after the laser heating.

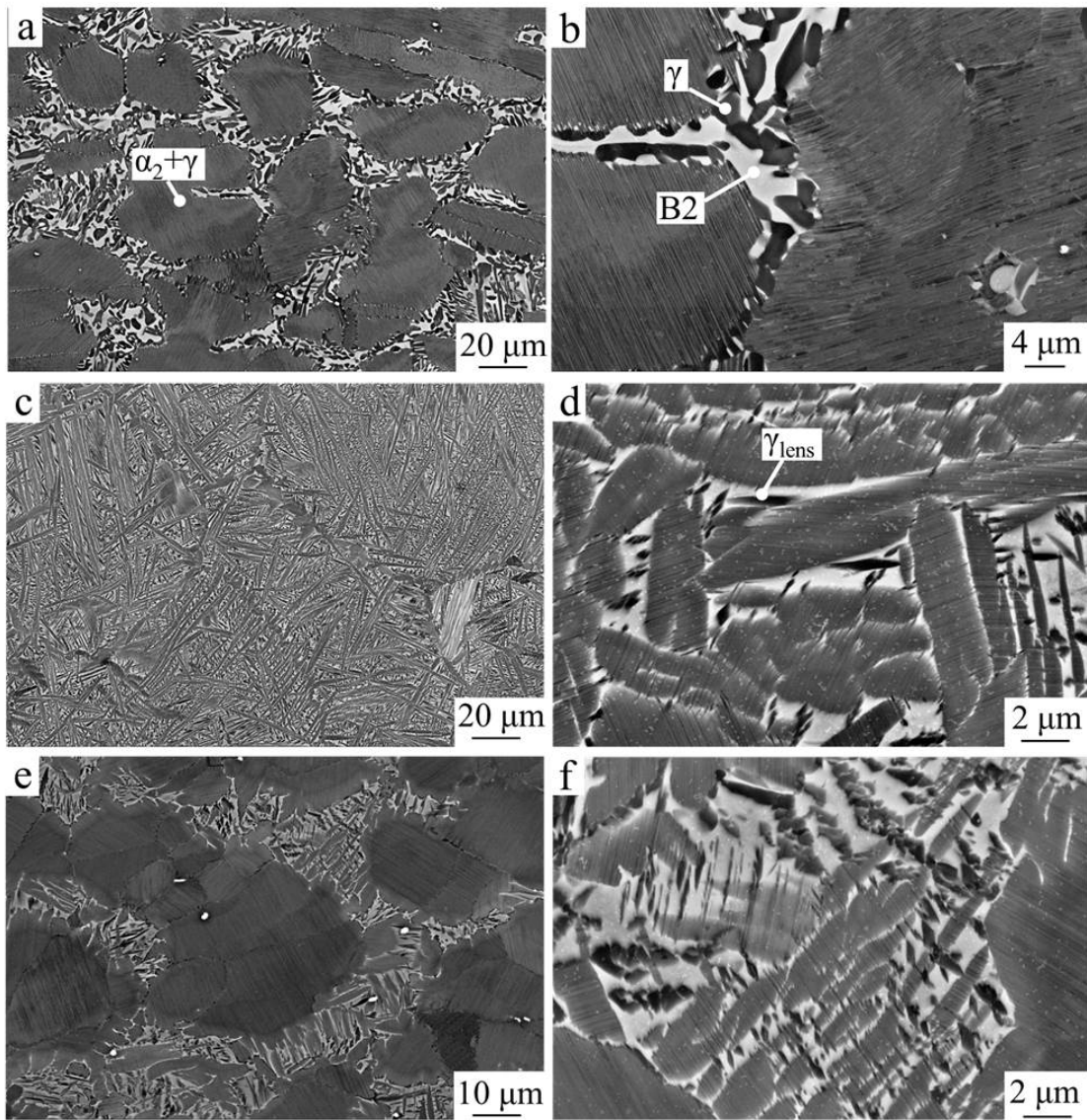


Fig. 4: The microstructure of the specimen #1, overview of (a) BM, (c) WZ and (e) HAZ and the areas of interest are enlarged to show the details of (b) BM, (d) WZ and (f) HAZ.

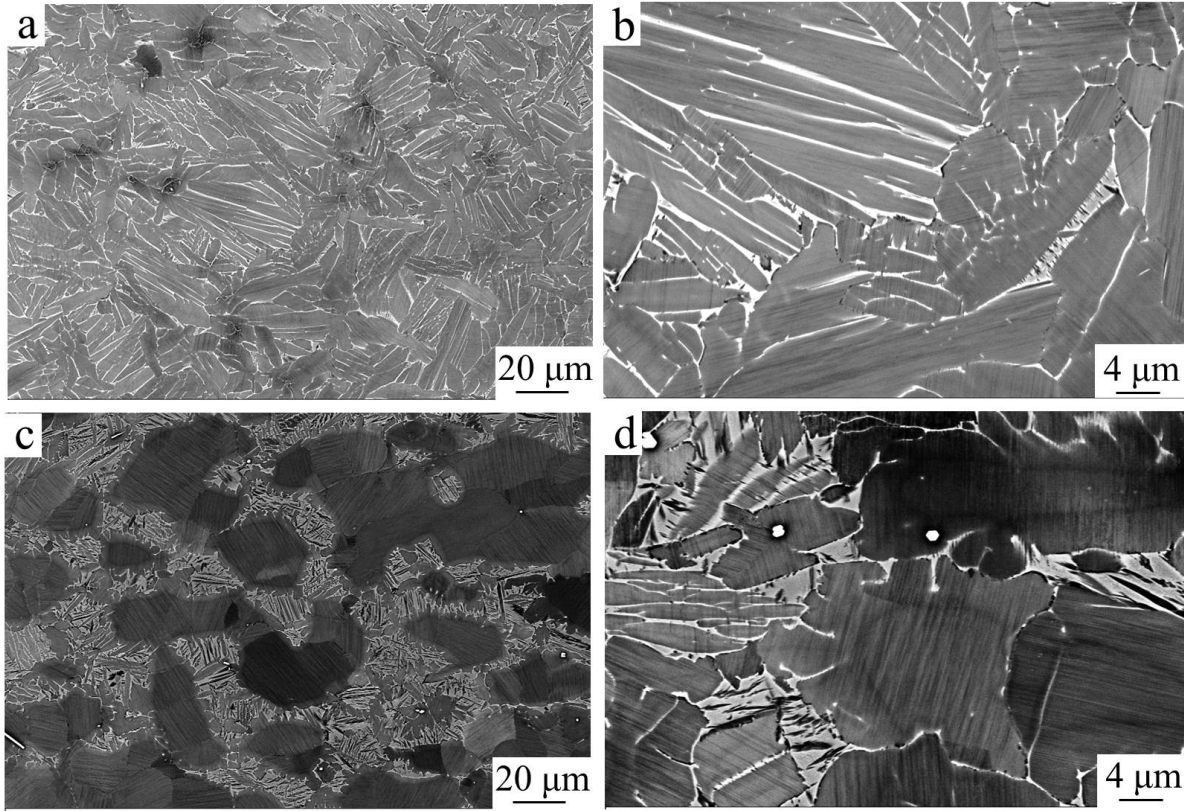


Fig. 5: The microstructure of the specimen #2, overview of (a) WZ and (c) HAZ. The areas of interest are enlarged to show the details of (b) WZ and (d) HAZ.

### 3.3 Residual stresses and phase analysis

It is assumed that the welding-induced residual stresses are responsible for the high cracking probability of the welded specimens. A plane stress state was assumed in the thin sheets for evaluation of stresses from strains determined in the directions parallel and perpendicular to the weld. The integrated diffraction patterns were fitted with a Gauss function and the scattering angle  $2\theta$  is related to the lattice distance  $d$  by

$$d = \lambda / (2 \sin \theta) \quad (2)$$

Variations of the stress-free interplanar lattice distance  $d_0$ , which is determined for the calculation of absolute stress value of the material, due to chemical composition changes were accounted for with the reference sample.

The strain  $\varepsilon$  was related to the lattice distance in weld piece and comb with the function of

$$\varepsilon = d / d_0 - 1 \quad (3)$$

The mean residual stresses were calculated by weighting with the phase volume fraction of  $\gamma$ ,  $\alpha_2$  and B2.

The residual stresses in the longitudinal direction (LD) and transverse direction (TD) to the weld are plotted for specimen #1 and specimen #2. In Fig. 6a, the longitudinal stress shows a symmetric morphology to the welding centre, where the highest tensile stress of 218 MPa is observed at the outer range of the WZ in specimen #1. As approaching to the welding centre, there is a sudden decrease of the tensile stress to 95 MPa, which forms a two-peak morphology in the WZ. The tensile stress changes sign into a longitudinal compressive stress in the HAZ at a distance of around  $\pm 2$  mm

from the weld centre to balance the high residual tensile stresses in the weld. The transverse stress is much lower in its amplitude and it also shows two-peak morphology. There are two maximum tensile stresses of 89 MPa at  $\pm 1.5$  mm from the centre, while this tension drops close to zero when it is at the centre of the weld zone and in the BM.

Fig. 6b presents the stress after a heat treatment via a defocused laser. The residual stresses are largely reduced to the maximum tensile stresses of 83 MPa and 32 MPa in both LD and TD, respectively. It indicates that post-weld heating via a defocused laser has a great influence on reducing the residual stress.

As the phase composition is essential for the quality of final welded piece, the phase distribution across the welding plate was determined. The content of the phases was calculated with the Rietveld method. Fig. 6c shows that the phase composition of the base material is consistent, with 13 vol.%  $\alpha_2$ , 18 vol.% B2 and 69 vol.%  $\gamma$  in the rolled sheet. This composition is strongly changed in the WZ. In sample #1, the amount of  $\alpha_2$  increases 3 times as in BM, to a volume fraction of 45 %. It overweighs  $\gamma$  and B2 phases, which account for 28 vol.% and 27 vol.%, respectively. However, the  $\alpha_2$  amount drops suddenly from 38 vol.% to 17 vol.% at the interface of the WZ and HAZ. Correspondingly, the  $\gamma$  content increases from 39 vol.% to 65 vol.%. It is worth to mention that there is a slight increase of  $\alpha_2$  phase at the position of  $\pm 3$  mm, which is the edge of the HAZ. It can be inferred that this area suffers a high cooling rate as a result of better heat conduction relative to the comparatively cold base material. The content of the B2 phase presents a small peak at the WZ centre, and remains almost constant at HAZ, with an average value of 16 vol.%.

In sample #2 (Fig. 6d), the amount of  $\alpha_2$  is decreased in the welding centre by the post-weld laser heat treatment. The WZ consists of 45 vol.%  $\gamma$ , balanced by 39 vol.%  $\alpha_2$ , and 16

vol.% B2 phase. Also, the width of the HAZ is effectively expanded to  $\pm 4.5$  mm. In the region of HAZ, the  $\alpha_2$  phase decreases continuously to 13 vol.% at a low gradient compared with Fig. 6c. The amount of B2 phase is reduced from 27 vol.% in the as-welded WZ to 16 vol.% after heat treatment. The reason of B2 phase reduction can be explained by the temperature curve measured during laser heating. The peak temperature of the WZ is 1282 °C, which is near the B2 minimum temperature as shown in Fig. 1b. The amount of B2 remains when the specimen cools down.

Both longitudinal and transverse stresses decrease at the welding centre in both specimens. A high fraction of B2 phase is observed at the same position of this stress valley. It is reported that at high temperature,  $\beta$  can be deformed more easily than  $\alpha_2$  and  $\gamma$  because of its bcc structure [18]. Since dislocation slip is easier in  $\beta$  grains than in  $\gamma$  and  $\alpha_2$ , the presence of the soft  $\beta$  is obviously beneficial in reducing the stress at grain boundaries. The high local stress can be relieved by the emission of dislocation into adjacent  $\beta$  grains. Thus, the high amount of B2 is helpful to reduce the residual stress at the welding centre.

### 3.4 Tensile test

The specimen #1 and #2 are tensile tested at both room temperature and 750 °C. All specimens failed in the WZ. The as-welded specimen shows higher ultimate tensile stress (UTS) compared to laser treated welds. Moreover, after heat treatment, the elongation to fracture is improved. The  $\alpha_2$  and B2 phases are reported to be brittle at RT and promote fracture of the specimen. Thus, the elongation can be improved by the reduction of the  $\alpha_2$  and B2 phases. However, at 750 °C B2 phase becomes ductile and improves the ductility at an expense of small reduction of UTS.

**THE COOLING GRADIENT AND MICROSTRUCTURE CONTROL IN LASER BEAM WELDED TIAL ALLOY ASSISTED BY TEMPERATURE FIELD SIMULATION**

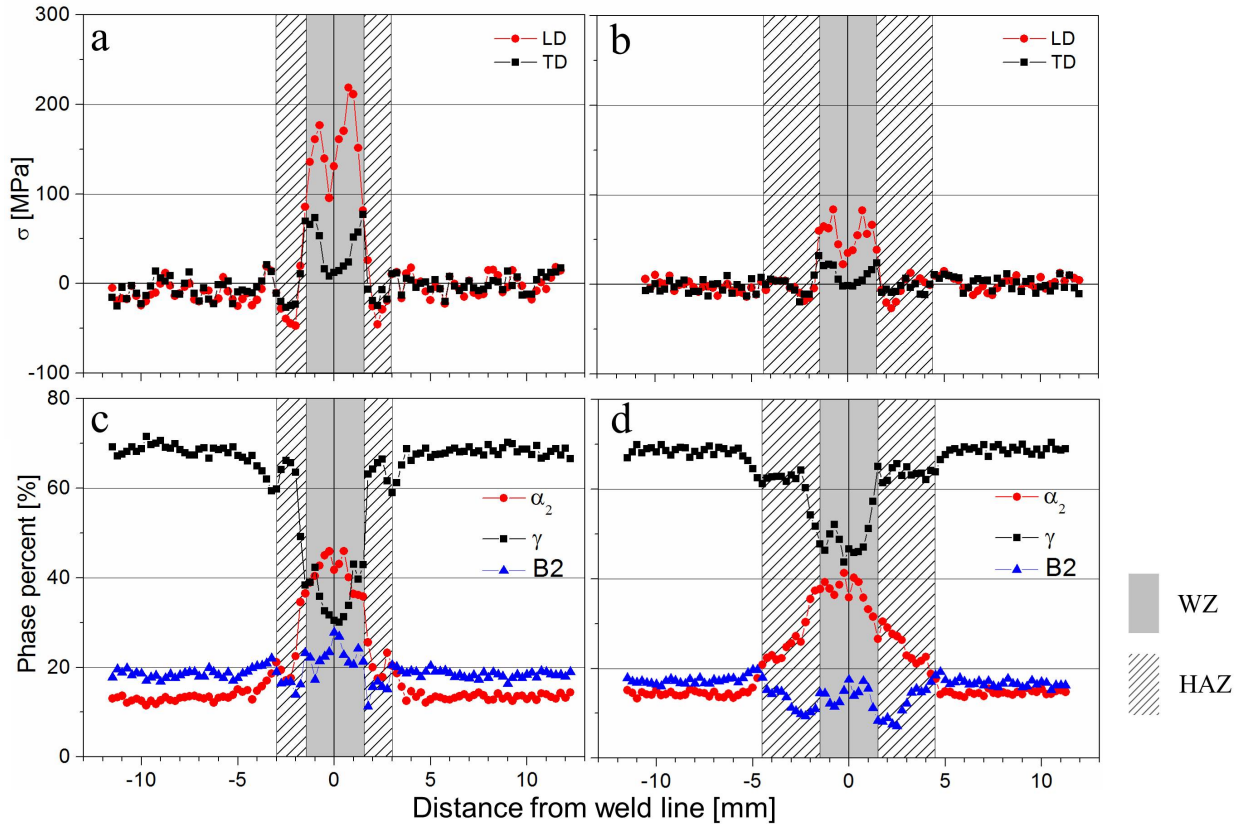


Fig. 6: The residual stress in the LD and TD in specimen (a) #1 and (b) #2. The volume fraction of the phases in specimen (c) #1 and (d) #2. The grey area is the WZ with a width of 3 mm. The patterned area is the HAZ. It shows a width of 6 mm in #1 and 9 mm in #2. The white area is the BM.

Table 1: Tensile properties of the specimen #1 and #2 at RT and 750 °C.

Temperature	RT			750 °C		
	BM	#1	#2	BM	#1	#2
UTS /MPa	967	936	911	805	782	768
Elongation /%	0.82	0.72	0.78	2.33	2.2	2.24

#### 4 Conclusions

The influence of the heating cycle on the cooling rates and hence on the mechanical/microstructural properties has been studied. Assisted by the temperature measurement and finite element simulation, the heating temperature and cooling rate in the WZ and HAZ are properly controlled, which leads to reduced residual stress and balanced mechanical properties. The B2 phase is reported as a ductile phase at high temperature and relieves the

residual stress by assisting the dislocation movement. This leads to the two-peak morphology of the residual stress. As the brittle  $\alpha_2$  and B2 phases are detrimental to the RT ductility, they are heat treated via a defocused laser to 1282 °C, where amount of  $\beta$  is minimised. After cooling down to 900 °C at a gradient of 59.2 °C/s, both phases are largely reduced in the WZ. The specimens show a microstructure with balanced strength and elongation at both RT and 750 °C.

## 5 Acknowledgements

The authors thank Mr. Manfred Horstmann and Mr. Hamdi Tek for carrying out the micro tensile test.

## 6 References

- [1] Clemens H, Kestler H. Processing and applications of intermetallic gamma-TiAl-based alloys. *Advanced Engineering Materials*, Vol. 2, pp 551-570, 2000.
- [2] Yamaguchi M, Inui H, Ito K. High-temperature structural intermetallics. *Acta Materialia*, Vol. 48, pp 307-322, 2000.
- [3] Appel F, Paul JDH, Oehring M. *Gamma titanium aluminide alloys science and technology*. Weinheim: WILEY-VCH, 2011.
- [4] Appel F, Wagner R. Microstructure and deformation of two-phase  $\gamma$ -titanium aluminides. *Materials Science and Engineering: R*, Vol. 22, pp 187-268, 1998.
- [5] Noda T. Application of cast gamma TiAl for automobiles, *Intermetallics*, Vol. 6, pp 709-713, 1998.
- [6] Chen GQ, Zhang BG, Liu W, Feng JC. Crack formation and control upon the electron beam welding of TiAl-based alloys. *Intermetallics*, Vol 19, pp 1857-1863, 2011.
- [7] Chaturvedi MC, Xu Q, Richards NL. Development of crack-free welds in a TiAl-based alloy. *Journal of Materials Processing Technology*, Vol 118, pp 74-78, 2001.
- [8] Liu J, Ventzke V, Staron P, Schell N, Kashaev N, Huber N. Effect of Post-weld Heat Treatment on Microstructure and Mechanical Properties of Laser Beam Welded TiAl-based Alloy, *Metallurgical and Materials Transactions A*, Vol. 45, pp 16-28, 2014.
- [9] Liu J, Ventzke V, Staron P, Schell N, Kashaev N, Huber N. Investigation of In Situ and Conventional Post-Weld Heat Treatments on Dual-Laser-Beam-Welded  $\gamma$ -TiAl-Based Alloy, *Advanced Engineering Materials*, Vol. 14, pp 923-927, 2012.
- [10] Arenas MF, Acoff VL. The effect of postweld heat treatment on gas tungsten arc welded gamma titanium aluminide, *Scripta Materialia*, Vol. 46, pp 241-246, 2002.
- [11] Schwaighofer E, Clemens H, Mayer S, Lindemann J, Klose J, Smarsly W, Guther V. Microstructural design and mechanical properties of a cast and heat-treated intermetallic multi-phase gamma-TiAl based alloy, *Intermetallics*, Vol. 44, pp 128-140, 2014.
- [12] Paradowska A, Finlayson TR, Price JWH, Ibrahim R, Steuwer A, Ripley M. Investigation of reference samples for residual strain measurements in a welded specimen by neutron and synchrotron X-ray diffraction. *Physica B: Condensed Matter*, Vol. 385-386, pp 904-907, 2006.
- [13] Schnubel D, Huber N. Retardation of fatigue crack growth in aircraft aluminium alloys via laser heating – Numerical prediction of fatigue crack growth. *Computational Materials Science*, Vol. 65, pp 461-469, 2012.
- [14] Cheng TT. The mechanism of grain refinement in TiAl alloys by boron addition - an alternative hypothesis. *Intermetallics*, Vol. 8, pp 29-37, 2000.
- [15] Hecht U, Witusiewicz V, Drevermann A, Zollinger J. Grain refinement by low boron additions in niobium-rich TiAl-based alloys. *Intermetallics*, Vol. 16, pp 969-978, 2008.
- [16] Oehring M, Stark A, Paul JDH, Lippmann T, Pyczak F. Microstructural refinement of boron-containing beta-solidifying gamma-titanium aluminide alloys through heat treatments in the beta phase field. *Intermetallics*, Vol. 32, pp 12-20, 2013.
- [17] Liu J, Dahmen M, Ventzke V, Kashaev N, Poprawe R. The effect of heat treatment on crack control and grain refinement in laser beam welded beta-solidifying TiAl-based alloy. *Intermetallics*, Vol. 40, pp 65-70, 2013.
- [18] Nieh TG, Wadsworth J. Fine structure superplastic intermetallics. *International Materials Reviews*, Vol. 44, pp 59-75, 1999.

## 7 Contact Author Email Address

mailto: jie.liu@hzg.de

## 8 Copyright Statement

The authors confirm that they, and/or their company or organization, hold copyright on all of the original material included in this paper. The authors also confirm that they have obtained permission, from the copyright holder of any third party material included in this paper, to publish it as part of their paper. The authors confirm that they give permission, or have obtained permission from the copyright holder of this paper, for the publication and distribution of this paper as part of the ICAS 2014 proceedings or as individual off-prints from the proceedings.